$IrGe_4$: A Predicted Weyl-Metal with a Chiral Crystal Structure

Callista M. Skaggs,[1,#] Dong-Choon Ryu,[2,3,#] Hari Bhandari,[4,5] Yan Xin,[6] Chang-Jong Kang,*[,2,3] Saul H. Lapidus,[7] Peter E. Siegfried,[4,5] Nirmal J. Ghimire,[4,5] Xiaoyan Tan,*[,1]

[1]*Department of Chemistry and Biochemistry, George Mason University, Fairfax, Virginia 22030, United States*

[2]*Department of Physics, Chungnam National University, Daejeon 34134, Republic of Korea*

[3]*Institute of Quantum Systems, Chungnam National University, Daejeon 34134, Republic of Korea*

[4]*Department of Physics and Astronomy, George Mason University, Fairfax, Virginia 22030, United States*

[5]*Quantum Science and Engineering Center, George Mason University, Fairfax, Virginia 22030, United States*

[6]*National High Magnetic Field Laboratory, Tallahassee, Florida 32310, United States*

[7]*Advanced Photon Source, Argonne National Laboratory, Argonne, Illinois 60439, United States*

[#]*Callista M. Skaggs and Dong-Choon Ryu contribute equally*

ABSTRACT

Polycrystalline $IrGe_4$ was synthesized by annealing elements at 800 °C for 240 h, and the composition was confirmed by energy-dispersive X-ray spectroscopy. $IrGe_4$ adopts a chiral crystal structure (space group $P3_121$) instead of a polar crystal structure ($P3_1$) that was corroborated by the convergent-beam electron diffraction and Rietveld refinements using the synchrotron powder X-ray diffraction data. The crystal structure features layers of $IrGe_8$ polyhedra along the *b* axis, and layers are connected by edge- and corner-sharing. Each layer consists of corner-shared [Ir_3Ge_{20}] trimers, which are formed by three $IrGe_8$ polyhedra connected by edge-sharing. Temperature-dependent resistivity indicates a metallic behavior. The magnetoresistance increases with increasing applied magnetic field, and the nonsaturating magnetoresistance reaches 11.5 % at 9 T and 10 K. The Hall resistivity suggests that holes are the majority carrier type with the carrier concentration of 4.02×10^{21} cm^{-3} at 300 K. Electronic band structures calculated by the density functional theory reveal a Weyl point with a chiral charge of +3 above the Fermi level.

INTRODUCTION

Topological materials such as Weyl metals/semimetals, Dirac metals/semimetals, and topological insulators have been studied intensively due to their interesting and novel physical properties, topological electronic band structures, and promising applications in spintronics, thermoelectrics, and energy-harvesting areas.[1] Weyl metals feature nontrivial electronic bands with valence and conduction bands that cross in isolated points (Weyl nodes) where spin-polarized bands disperse linearly, giving rise to novel electronic properties such as magnetic monopoles in bulk and Fermi arcs in the surface, making these materials different from ordinary metals. When Weyl nodes ideally locate at the Fermi level, the Weyl fermions can lead to unique magnetoelectric properties such as chiral anomaly,[2,3,4,5] and anomalous Hall effect observable in transport measurements.[6]

Reported Weyl metals/semimetals include MPn (M = Ta, Nb; Pn = P, As; space group $I4_1md$),[4,7,8,9] MTe_2 (M = W, Mo; $Pnm2_1$),[10,11] $HgCr_2Se_4$ ($Fd\bar{3}m$),[6] Co_2MnA (A = Al, Ga, $Fm\bar{3}m$),[12,13] RAlX (R = La, Ce, Pr, Nd; X = Si, Ge; $I4_1md$),[14,15] CoSi ($P2_13$),[16] HfCuP ($P3m1$),[17] EuAgP ($P6_3/mmc$),[18] EuB_6 ($Pm\bar{3}m$),[19] $EuMnSb_2$ ($Pnma$),[20] $YbMnBi_2$ ($P4/nmm$),[21] Mn_3X (X = Ge, Sn; $P6_3/mmc$),[22,23] $Co_3Sn_2S_2$ ($R\bar{3}m$),[24] and $MIrTe_4$ (M = Ta, Nb; $Pmn2_1$).[25,26] Non-magnetic Weyl metals/semimetals adopt the non-centrosymmetric (NCS) crystal structure with inversion-symmetry broken (note that magnetic Weyl metals/semimetals can be NCS or centrosymmetric), which also provides opportunities to study the nonlinear optoelectronic

phenomena and even ferroelectric switching in thin layers. For example, NCS Weyl semimetal $TaIrTe_4$ shows wireless radiofrequency rectification related to the nonlinear Hall effect, and $NbIrTe_4$ exhibits colossal terahertz topological response.[25,26] Apart from $MIrTe_4$ (M = Ta, Nb), there are no other NCS Ir-containing Weyl or Dirac metals/semimetals. Considering all crystal structures, there are only a few Ir-containing intermetallics reported to be Weyl or Dirac metals/semimetals, including Ir_2In_8Q (Q = S, Se, Te; $P4_2/mnm$) with a large nonsaturating transverse magnetoresistance (MR),[27,28] and $Ir_{1-x}Pt_xTe_2$ ($0.1 < x < 0.4$, $P\bar{3}m1$) even showing a superconducting state.[29,30] Inspired by these intriguing reports, we are motivated to discover more Ir-containing topological materials with the NCS crystal structure.

Among the reported binary Ir-Ge compounds, IrGe ($Pnma$)[31], Ir_4Ge_5 ($P\bar{4}c2$),[32,33] and Ir_3Ge_7 ($Im\bar{3}m$)[34] adopt centrosymmetric space groups, while $IrGe_4$ has been reported to form two possible NCS space groups, $P3_1$ (No. 144, both polar and chiral) and $P3_121$ (No. 152, chiral).[35,36] The electronic band structure of $IrSn_4$ with the space group $P3_121$ indicates the existence of Kramers-Weyl fermions, but there is a lack of the electronic band structure of $IrGe_4$.[37] In addition, the physical properties of most Ir-Ge compounds are barely studied except for IrGe, which shows strong electron-phonon coupling and superconducting transition at 4.7 K.[38,39] Therefore, in this study, we will investigate the crystal structure, electronic band structures, and physical properties of $IrGe_4$.

EXPERIMENTAL SECTION

Starting Materials and Synthesis. $IrGe_4$ polycrystalline samples were synthesized using the solid-state method with a stoichiometric ratio. Starting materials of Ir powder (99.9% mass fraction, Alfa Aesar) and Ge powder (99.999% mass fraction, Alfa Aesar) were weighed, ground thoroughly, and pressed into a pellet (diameter = 6 mm) inside an argon-filled glove box (O_2% < 1 ppm, H_2O% < 1 ppm). The obtained pellet was transferred into an open-ended quartz tube that was sealed with an oxygen /natural gas torch under a dynamic vacuum (< 10^{-3} Torr). The sealed tube was heated in a box furnace from room temperature to 800 °C with a ramp time of 48 h, kept at that temperature for 240 h, and then the furnace was cooled to room temperature within 48 h. A dense pellet (> 91% density, diameter = 4.53 mm, height = 3.14 mm) was prepared by pressing $IrGe_4$ powders at 4 GPa at room temperature using a Walker-type high-pressure press. During the sample preparation, no uncommon hazards were noted.

Laboratory and Synchrotron Powder X-ray Diffraction. Powder X-ray diffraction (PXRD) patterns of polycrystalline samples were collected using a benchtop Miniflex-600 powder X-ray diffractometer (Cu Kα, λ =1.5418 Å). The PXRD data were collected at room temperature for 1 h with a scattering angle 2θ ranging from 10 to 70°. Synchrotron PXRD patterns were obtained ($0.5° < 2\theta < 36°$) with λ = 0.458073 Å at the 11-BM beamline at the Advanced Photon Source, Argonne National Laboratory. Rietveld refinements of the synchrotron PXRD data were carried out with the suite of FullProf programs.[40]

Transmission Electron Microscopy (TEM). TEM experiments were carried out with a probe aberration-corrected sub-Å resolution JEOL JEM-ARM200cF microscope at 200 kV. Polycrystalline $IrGe_4$ powders were ground into thin electron-transparent pieces and loaded onto a carbon-coated 200-mesh Cu TEM grid. Selected area electron diffraction (SAED) patterns and corresponding atomic resolution high-angle-annular-dark-field scanning transmission electron microscopy (HAADF-STEM) images were collected on a single crystal piece. Convergent-beam electron diffraction (CBED)

patterns were obtained by focusing the electron beam onto the crystal surface into several tens of nanometer diameter areas in the TEM nano-diffraction mode.

Chemical Analysis. Elemental analysis of $IrGe_4$ was performed on thin pellets with a JEOL JSM-IT500HRLV scanning electron microscopy (SEM) and an accessory Octane Elect Plus energy-dispersive X-ray (EDX) spectroscopy system. The SEM images and elemental maps were collected with an accelerating voltage of 15 kV.

Physical Properties. $IrGe_4$ with the Quantum Design DynaCool physical property measurement system (PPMS). A 4-probe method with 25 μm Pt wires was used for resistivity, MR, and Hall measurements with an excitation current of 4 mA. The Pt wires were affixed on the dense pellet with Epotek H20E silver epoxy. Temperature-dependent resistivity data were collected between 1.8 and 300 K with the applied magnetic field (B) at 0 and 9 T. Isothermal field-dependent Hall resistivity and MR were measured between 10 and 300 K with varying B up to ± 9 T.

Density Functional Theory (DFT) Calculations. DFT calculations were performed using the projector augmented wave band method implemented in VASP.[41,42,43] The generalized-gradient approximation (GGA) of Perdew-Burke-Ernzerhof (PBE) was adopted for the exchange-correlation functional.[44] Experimental crystal structure (Table 1) was employed for the DFT calculations. A 10 x 10 x 10 k-point mesh was used for the Brillouin zone integration. A plane wave cutoff energy of 400 eV was selected, and a convergence criterion of 10^{-8} eV was applied. Spin-orbit coupling (SOC) is taken into account in a second variation method. Wannier90 and WannierTools programs were used to calculate the chiral charge of Weyl points.[45,46] In order to preserve symmetries imposed in the crystal structure during the Wannierization, the symmetrized Wannier method was adopted.[47]

RESULTS AND DISCUSSION

Synthesis and Crystal Structure. The polycrystalline $IrGe_4$ samples were prepared using the solid-state method based on a similar heating profile reported in 1969.[35] The PXRD pattern of the obtained sample matches the theoretical patterns of $IrGe_4$ crystallizing in trigonal crystal structures with space groups $P3_1$ (No. 144) and $P3_121$ (No. 152) as these two patterns are almost indistinguishable (Figure 1).

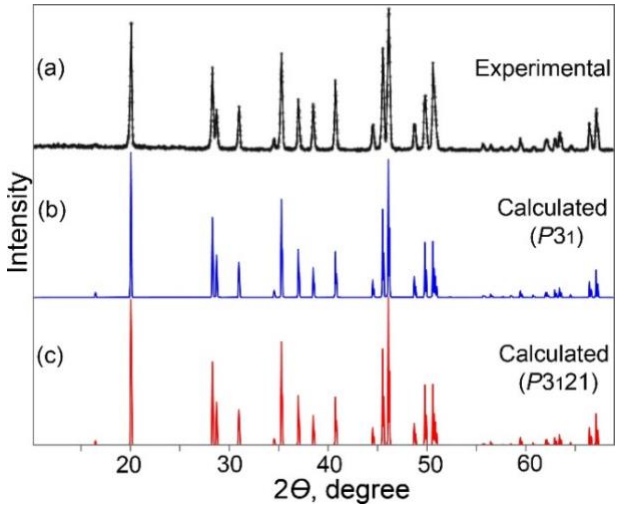

Figure 1. Experimental (a) and calculated PXRD patterns of $IrGe_4$ with space groups $P3_1$ (b) and $P3_121$ (c).

In both structures, unit cell parameters are the same, and Ir atoms occupy the same Wyckoff site 3a (Table 1). In the polar and chiral crystal structure (space group $P3_1$), there are four Ge sites (3a, 3a, 3a, 3a), while the chiral crystal structure (space group $P3_121$) only has three Ge sites (3b, 3b, 6c). The polar and chiral crystal structure can be viewed as the splitting of the 6c site in the chiral crystal structure into two 3a sites. The arrangement of $IrGe_8$ polyhedra and the perspective view of two crystal structures are the same (Figures 2 and S1), but the Ir-Ge bond distances in $IrGe_8$ polyhedra are different due to the different sites and symmetry (Table 2). Figure 2 shows the chiral crystal structure (space group $P3_121$), which consists of layers of $IrGe_8$ polyhedra when viewed along the *b* axis (Figure 2a). In each layer, three $IrGe_8$ polyhedra share Ge1-Ge2 edges and form $[Ir_3Ge_{20}]$ trimers (Figure 2d), which are corner-shared via Ge3 atoms (Figure 2b). Between layers of $[Ir_3Ge_{20}]$ trimers, one $IrGe_8$ polyhedron is edge-sharing, and the other two $IrGe_8$ polyhedra are corner-sharing (Figure 2c). The same connection of $IrGe_8$ polyhedra in the polar and chiral crystal structure (space group $P3_1$) is shown in Figure S1. The Ge3 (6c) atoms in Figure 2 correspond to Ge1 (3a) and Ge2 (3a) atoms in Figure S1, while Ge1 (3b) and Ge2 (3b) atoms in Figure 2 correspond to the Ge3 (3a) and Ge4 (3a) atoms in Figure S1, respectively. More discussion on symmetry elements between the two structures is shown in the TEM section.

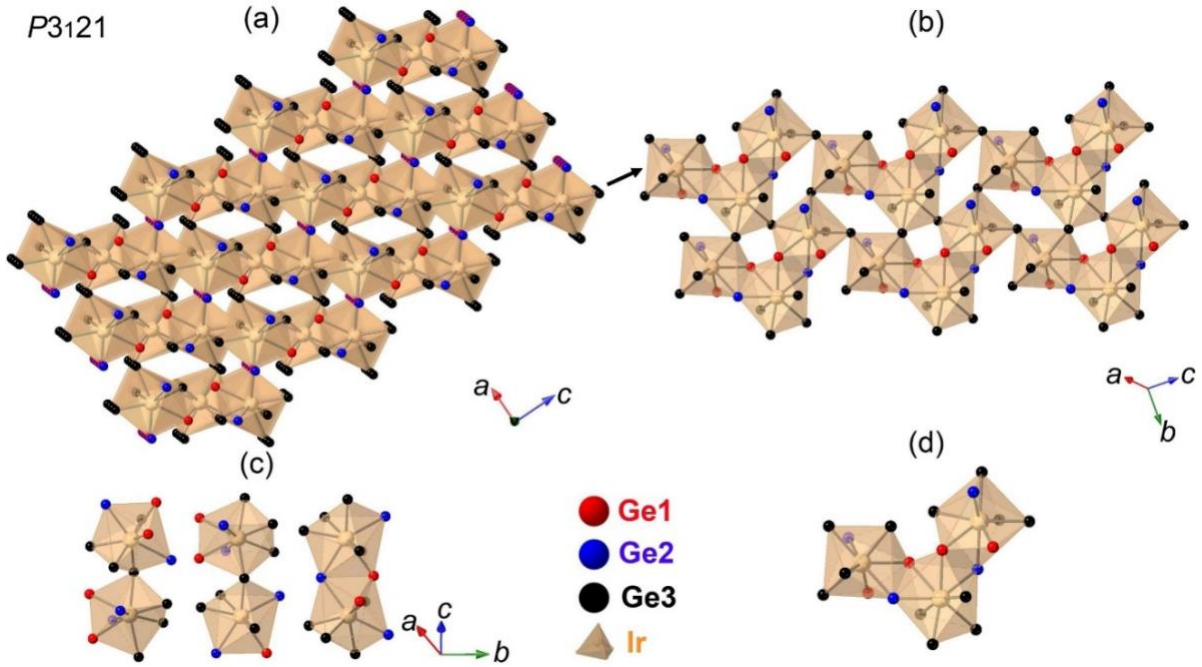

Figure 2. Perspective view of the chiral crystal structure of $IrGe_4$ (space group $P3_121$) along the *b* axis (a), one layer of $[Ir_3Ge_{20}]$ trimers by tilting *b* axis (b), edge-sharing and corner-sharing connection of $IrGe_8$ polyhedral between layers (c), and one isolated $[Ir_3Ge_{20}]$ trimer (d).

Rietveld refinements were carried out using the room-temperature synchrotron PXRD data. Both crystal structures with space groups $P3_1$ and $P3_121$ were employed as the initial models. The overall fitting and selected structural parameters of Rietveld refinement results are presented in Figure 3 and Table 1. The data can fit well with both models, as indicated by the similar Rietveld refinement criteria of fit. The refined unit cell parameters were $a = b = 6.2132(1)$ Å, $c = 7.7848(1)$ Å, $V = 260.263(1)$ Å^3, which are close to the previously reported values, $a = b = 6.215(5)$ Å, $c = 7.784(2)$ Å, $V = 260.385(1)$ Å^3.[35] The

refined sites are very close to the reported values as well. Careful examination of the high-resolution synchrotron PXRD pattern identifies very weak reflections at $2\Theta = 7.4°$, 10.5°, 11.3°, 12.9°, and 14.9° (the first strong peak is marked with an asterisk in Figure 3), which are due to a small amount of Ir_3Ge_7 (< 0.4%) impurity.

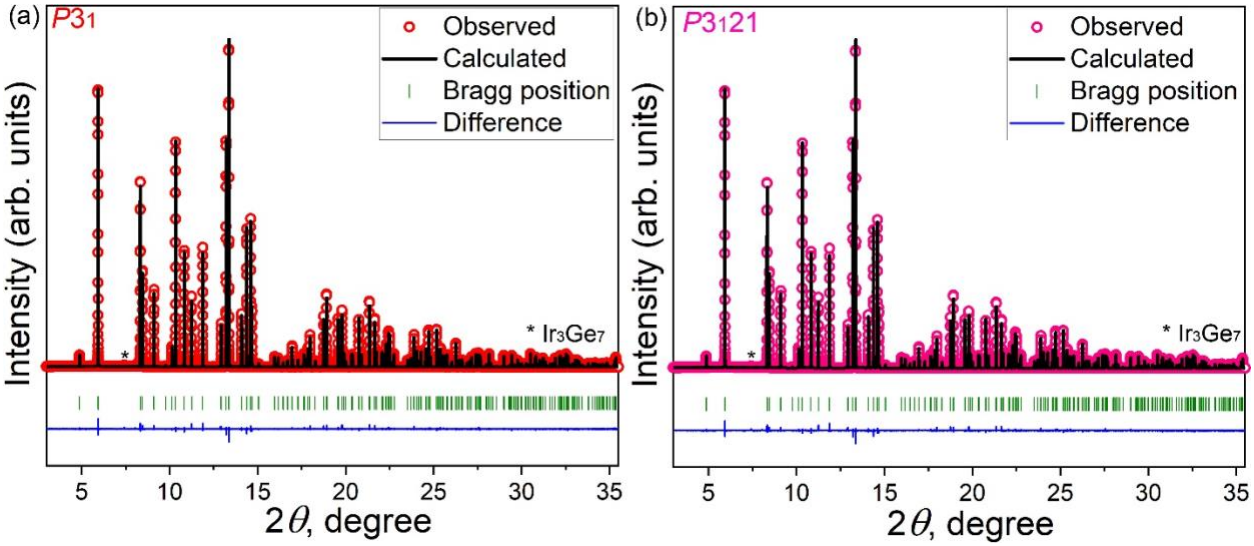

Figure 3. Rietveld refinements of synchrotron PXRD data ($\lambda = 0.458073$ Å) of $IrGe_4$ with space groups $P3_1$ (a) and $P3_121$ (b). The observed data (red), calculated pattern (black), expected Bragg peak positions (green), and the difference between those two patterns (blue) are provided. Asterisk (*) represents the first strong reflection of Ir_3Ge_7 impurity.

Table 1. Selected Structural Parameters of Rietveld Refinements of $IrGe_4$

sample		$IrGe_4$		$IrGe_4$	
space group, #		$P3_1$, No. 144		$P3_121$, No. 152	
temperature		300 K			
mol. wt., g/mol		482.78			
density (calculated), g/cm^3		9.237			
wavelength, Å		0.458073			
Z		3			
lattice parameters		$a = b = 6.2132(1)$ Å, $c = 7.7848(1)$ Å, $V = 260.263(1)$ Å^3 $\alpha = \beta = 90°$ $\gamma = 120°$			
Rietveld criteria of fit[a]		$R_p = 7.89\%$, $R_{wp} = 10.8\%$, $R_{exp} = 6.99\%$, $\chi^2 = 2.38$		$R_p = 7.96\%$, $R_{wp} = 10.8\%$, $R_{exp} = 6.99\%$, $\chi^2 = 2.4$	
site	Wyckoff symbol	x, y, z	site	Wyckoff symbol	x, y, z
Ir1	3*a*	0.3172(1), 0, 0.33(2)	Ir1	3*a*	0.3171(1), 0, 0.3333
Ge1	3*a*	0.4905(7), 0.2161(8), 0.05(3)	Ge3	6*c*	0.4861(1), 0.2191(1), 0.0523(1)
Ge2	3*a*	0.2221(8), 0.4820(7), 0.94(3)			
Ge3	3*a*	0.0783(2), 0, 0.82(3)	Ge1	3*b*	0.0783(1), 0, 0.8333
Ge4	3*a*	0.6181(2), 0, 0.82(3)	Ge2	3*b*	0.6178(2), 0, 0.8333

a. $R_{wp} = \sqrt{\frac{\sum_i w_i (y_i^{calc} - y_i^{obs})^2}{\sum_i w_i (y_i^{obs})^2}}$, $R_{exp} = \sqrt{\frac{N - P}{\sum_i w_i (y_i^{obs})^2}}$, $R_p = \sqrt{\frac{\sum_i (y_i^{calc} - y_i^{obs})^2}{\sum_i (y_i^{obs})^2}}$, $\chi^2 = (R_{wp}/R_{exp})^2$, where y_i^{calc} and y_i^{obs} are the calculated and observed intensities at the i^{th} data point, the weight w_i is $1/\sigma^2$ from counting statistics, with the same normalization factor, N is the number of measured data points. *P* represents the number of refined parameters.

The refined Ir-Ge bond distances (*d*) are listed in Table 2 and compared with previously published two crystal structures with space groups $P3_1$ and $P3_121$. The *d*(Ir-Ge) is between 2.48-2.64 Å, close to the previously determined values (2.43-2.65Å).[35] In the polar and chiral crystal structure (space group $P3_1$), eight Ir-Ge bond distances in each $IrGe_8$ polyhedron are different (between 2.48-2.64 Å), even though there are two pairs are very close, which makes the $IrGe_8$ polyhedron very distorted. In contrast, in the chiral crystal structure (space group $P3_121$), there are only four different Ir-Ge bond distances, which are between 2.49-2.60 Å. Therefore, the $IrGe_8$ polyhedron is more distorted in the both polar and chiral crystal structure than in the chiral only crystal structure. The bond distances observed in $IrGe_4$ are close to those reported in IrGe (2.47-2.69 Å),[31] Ir_4Ge_5 (2.27-2.83 Å),[32,33] Ir_3Ge_7 (2.52-2.58 Å),[34,48] $IrGe_{1.5}Te_{1.5}$ (2.55 Å),[49] Yb_2IrGe_2 (2.47-2.68 Å),[50] LuIrGe (2.51-2.58 Å),[50] and $Lu_3Ir_2Ge_3$ (2.46-2.63 Å).[50]

Table 2. Selected Bond Distances in $IrGe_4$

space group $P3_1$ bond-distance, Å			space group $P3_121$ bond-distance, Å		
Ir-Ge	this work	reported values[35]	Ir-Ge	this work	reported values[35]
Ir-Ge2	2.48(3)	2.432	Ir-Ge3	2.512(1)	2.493
Ir-Ge1	2.50(3)	2.525	Ir-Ge3	2.512(1)	2.493
Ir-Ge4	2.52(2)	2.529	Ir-Ge3	2.538(1)	2.530
Ir-Ge2	2.53(6)	2.543	Ir-Ge3	2.538(1)	2.530
Ir-Ge1	2.56(2)	2.550	Ir-Ge2	2.554(1)	2.583
Ir-Ge3	2.56(5)	2.543	Ir-Ge2	2.554(1)	2.583
Ir-Ge4	2.59(5)	2.645	Ir-Ge1	2.600(1)	2.601
Ir-Ge3	2.64(2)	2.649	Ir-Ge1	2.600(1)	2.601

TEM. To confirm whether $IrGe_4$ crystallizes in the $P3_1$ (polar and chiral) or $P3_121$ (chiral) space group that are indistinguishable based on PXRD patterns, TEM experiments were carried out on thin electron-transparent pieces prepared from polycrystalline $IrGe_4$ powder samples. The atomic resolution HAADF-STEM image was obtained from a crystal piece along [110] (Figure 4a). The brightest dots are the Ir atomic columns since the image contrast is roughly proportional to atomic number Z^2, and Ir is 77. The less bright spots are the Ge columns with a Z number of 34. The sketch of the crystal structure projected along [110] is shown in Figure 4b, with an enlarged image superimposed with the unit cell sketch showing the Ir and Ge atoms. As shown in Figure 4a, one particular Ge column that is in the middle of two vertical Ir columns shows a slightly brighter intensity than the rest of the Ge columns. These special Ge columns are indicated by darker blue circles in the superimposed blow-up image, with one pointed by a red arrow. The image intensity is also proportional to the number of atoms in the column. The reason for its higher intensity is that the atom density per unit length along [110] is higher for this particular column than others along the electron beam direction. The atom distance is smaller for this column (d = 3.313 Å) than other Ge columns (d =

6.215 Å). Thus, at the same sample thickness, there are more Ge atoms in that special column than the other Ge columns, resulting in a brighter intensity. The experimental image along [110] matches exactly the crystal structure of $IrGe_4$, but we can't distinguish the space group from the image. The selected area electron diffraction (SAED) pattern of $IrGe_4$ was obtained along the [110] zone axis with indexed planes of $(\bar{1}10)$, $(\bar{1}\bar{1}1)$, (001), etc., which are corresponding miller planes for both space groups $P3_1$ and $P3_121$ (Figure 4c).

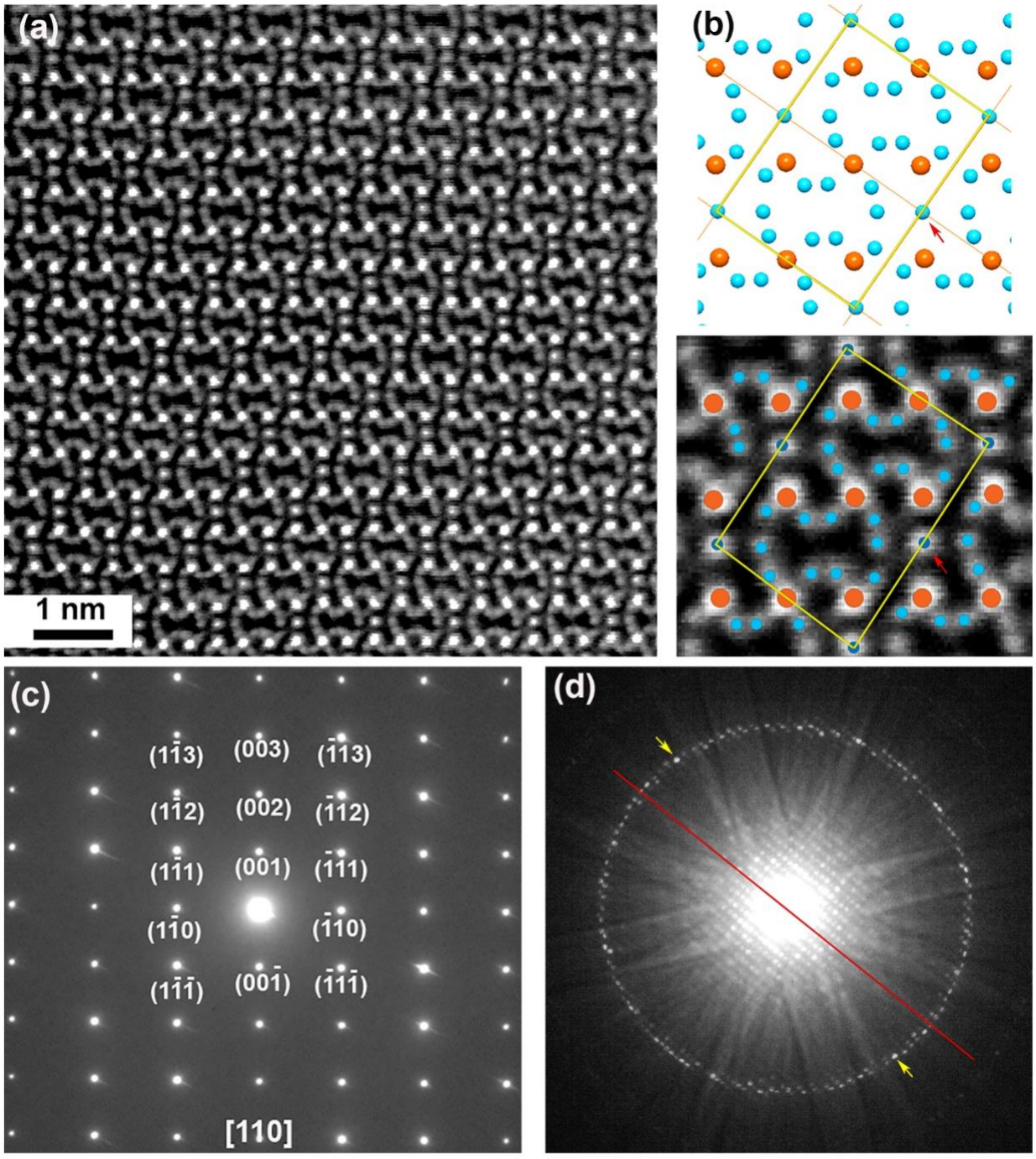

Figure 4. (a) Atomic resolution HAADF-STEM Z contrast image of $IrGe_4$ crystal along [110]. (b) Sketch of the crystal structure projected along [110]. The yellow rectangle box is the unit cell. Blow-up image superimposed with circles of

Ir (Orange) and Ge (blue) atoms. The red arrows point to the Ge columns with higher atom density. (c) [110] selected area electron diffraction pattern. (d) The whole pattern of [110] CBED. The red line and yellow arrows are guides for the eye.

CBED patterns can be useful in distinguishing 32 point groups due to dynamic scattering.[51,52,53] The space group $P3_1$ has the point group 3 and Laue class $\bar{3}$, while the space group $P3_121$ has point group 32, and Laue class 3m. It is known that for a [110] zone axis, the whole pattern (WP) of [110] CBED has a 2-fold rotation symmetry for $P3_121$ and no symmetry (1) for $P3_1$.[54] The WP CBED presented in Figure 4d shows a 2-fold rotation axis symmetry. If the pattern is rotated 180° along the axis perpendicular to the surface of the paper, the bright spots/disc on the upper side will coincide with the arrowed disc in the lower part, and other spots/discs are also exactly the same, i.e., the details of the pattern is exactly the same. Therefore, it means that the WP CBED has a 2-fold rotation axis, and we can determine that this $IrGe_4$ crystal has a space group of $P3_121$. Although we only looked at a few crystals, we believe that majority of the crystals have symmetry $P3_121$ as the single crystal piece is randomly selected from thousands of crystal pieces, which was thin enough and we were able to tilt to the right zone axis in the TEM. However, small amount of $P3_1$ phase might exit.

Chemical Analysis. Semi-quantitative SEM-EDX measurements were performed on an $IrGe_4$ dense pellet. The EDX maps of the surface of the $IrGe_4$ dense pellet indicate that Ir and Ge elements are homogeneously distributed through the pellet (Figure 5), with the molar ratio of Ir: Ge equal to 1: 4.01, which confirms the empirical chemical composition.

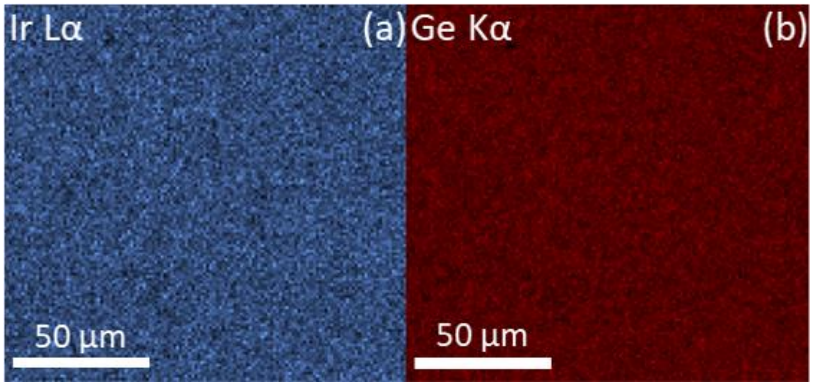

Figure 5. EDX elemental maps of the surface of an $IrGe_4$ dense pellet.

Physical Properties. The temperature-dependent resistivity was measured on an $IrGe_4$ dense pellet in zero external magnetic field as well as in a magnetic field of 9 T (Figure 6a). In each case, the resistivity decreases with decreasing temperature from 300 to 1.8 K, which suggests that $IrGe_4$ is a metal. However, the residual resistivity (resistivity at 1.8 K) is pretty large (576 and 642 μΩ·cm at 0 and 9 T, respectively). This may be due to grain boundaries in the pressed pellet and is likely the cause of a small residual resistivity ratio (RRR) = $\rho_{300K}/\rho_{1.8K}$ of 3.8 (for 0 T).

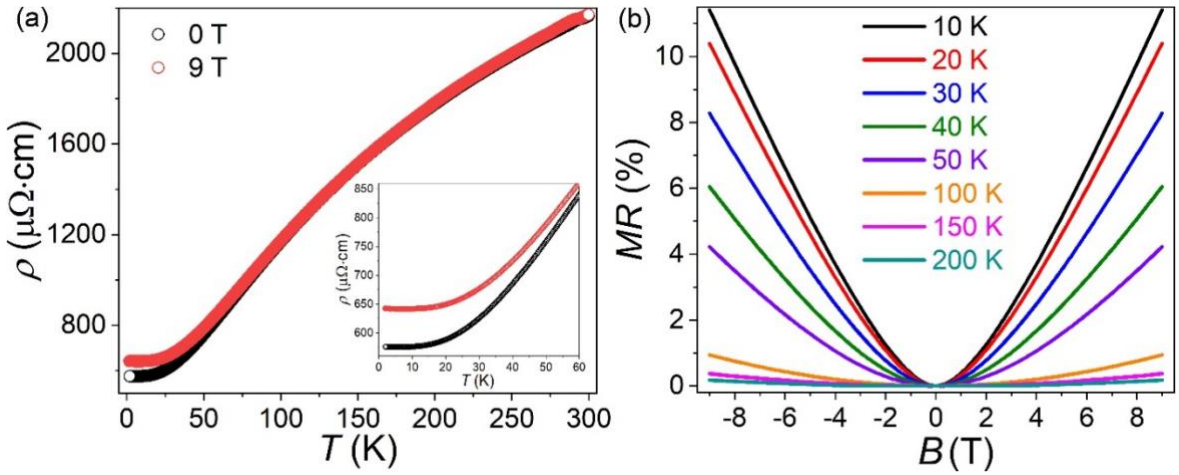

Figure 6. (a) Temperature-dependent resistivity of $IrGe_4$ with the low-temperature data (1.8, 60 K) as the inset, and (b) MR measured between 10 and 200 K.

The MR measurements were performed between 10 and 200 K. The MR is defined as $[(\rho_B - \rho_{0T})/\rho_{0T}] \times 100\%$, where ρ_B and ρ_{0T} are the resistivity measured with applied magnetic field B and B = 0 T, respectively. The isothermal MR is larger at low temperatures (Figure 6b). At all temperatures, the MR is quadratic in the magnetic field and remains unsaturated with a value of 11.5 % at 9 T and 10 K. During the process of submitting the manuscript, we noticed the recent report on single crystals of $IrGe_4$ (chiral space groups $P3_121$ and $P3_221$) showing larger RRR and MR values, and a superconducting transition at 1.1 K.[55]

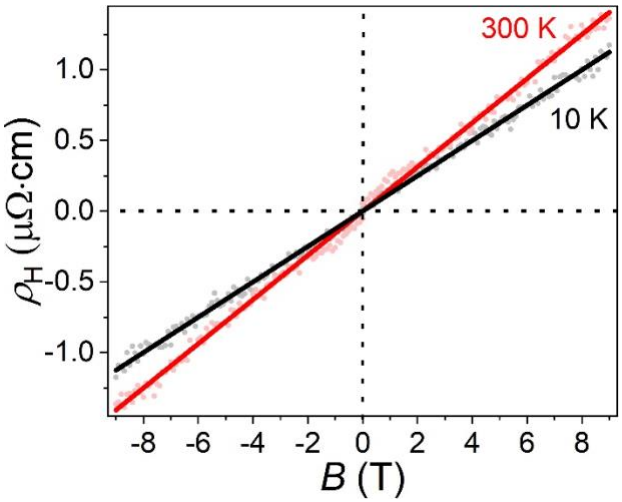

Figure 7. Hall resistivity of $IrGe_4$ measured at 10 and 300 K (solid lines are straight lines that fit the data).

Hall resistivity (ρ_H) measured between 10 and 300 K shows a linear behavior as a function of the magnetic field. In the entire temperature range (data shown only for 1.8 and 300 K in Figure 7) measured, ρ_H has a positive slope, indicating holes to be the majority carrier, consistent with the large hole pockets observed in the electron band structure shown later in the DFT calculations section. The carrier concentration (n_h) of holes can be estimated based on the equation, $n = 1/(eR_H)$, in which e is the charge of an electron and R_H is the Hall coefficient (the slope in Figure 7). The slope is 1.27×10^{-9} m^3/C

and 1.56 × 10^{-9} m^3/C, and the calculated n_h is 4.9 × 10^{21} cm^{-3} and 4.02 × 10^{21} cm^{-3} at 10 and 300 K, respectively, consistent with other bad metals such as $CoNb_3S_6$.[56]

DFT Calculations. Electronic structures of $IrGe_4$ were obtained within the DFT framework. Two different crystal structures with space groups of $P3_1$ (No. 144) and $P3_121$ (No. 152) were considered in the DFT calculations. Both $P3_1$ and $P3_121$ structures do not have inversion symmetry, but they have screw axes of 3_1 and 3_2 in the crystallographic notation, which are threefold rotation axes combined with translations of 1/3 and 2/3 along the c-axis direction, respectively. Hence, the two structures are NCS chiral structures.[57] However, the $P3_121$ structure has additional twofold rotation symmetry along the [110] axis, which is broken in the $P3_1$ structure due to Γ_2 symmetry distortion realized in a structural phase transition between the two structures (Figure 8).

The energy of the $P3_121$ structure is 3.3 meV/atom lower than that of the $P3_1$ one in the DFT calculations, which is consistent with the TEM results. However, it is noteworthy that there are DFT computational errors with a standard deviation of 24 meV/atom in the evaluation of energies.[58] Therefore, the energy difference of 3.3 meV/atom is insignificantly small, falling within the DFT error bar and even smaller than the room-temperature kT values of 26 meV. Consequently, the current DFT calculations cannot provide conclusive evidence regarding the true ground-state structure. Besides, due to the small energy difference, computed DFT electronic structures for the two structures are nearly identical. Here, the experimental refined crystal structure with the space group $P3_121$ (No. 144) was adopted for further theoretical analysis, especially for its topological nature.

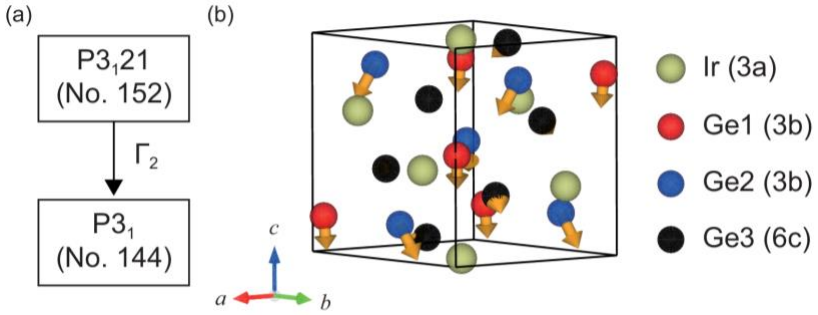

Figure 8. (a) Group-subgroup relation between two space groups of $P3_121$ (No. 152) and $P3_1$ (No. 144). The symmetry of atomic displacements is Γ_2, realized in the structural phase transition between the two space groups. (b) Atomic displacements of the Γ_2 symmetry in the $P3_121$ (No. 152) structure are presented by orange arrows.

The band structure of the crystal structure (space group $P3_121$) with SOC considered is provided in Figure 9a. The comparison of band structures without and with SOC is shown in Figure S2. Because $IrGe_4$ is a chiral crystal with non-magnetic order, it possesses symmetry-enforced Weyl points at time-reversal invariant momenta (TRIMs). These points are so-called Kramers-Weyl points, which were proposed in $IrSn_4$ (space group $P3_121$) based on theoretical considerations.[37] The band structure of $IrGe_4$ (space group $P3_121$) is very similar to that of $IrSn_4$ (space group $P3_121$). In addition, this system has many accidental Weyl points (non-Kramers) on generic k-points within an energy window of $|E - E_F| < 0.5$ eV in the Brillouin zone. Some of these points are illustrated in Fig. 9(a), while a complete display can be found in Figure S3. Hole pockets are shown near Γ-M, Γ-A, and A-H directions, while electron pockets are near L, but the larger hole pockets suggest that holes are the dominant carrier type, which is consistent with the positive slope shown in the Hall resistivity results (Figure 7). To

determine the chiral charges of the Kramers-Weyl points (or the Chern number), the Wilson loop method was used to calculate Wannier charge centers (WCC) within a small sphere centered at each Kramers-Weyl point, excluding other band crossing points in momentum space.[59] In other words, the chiral charge could be computed by integrating the Berry curvature over a closed surface of the corresponding small sphere. Therefore, Weyl points with positive or negative charges act as sources or sinks of the Berry curvature flux, respectively, in momentum space. It is equivalent to charged particles acting as sources or sinks of electric flux in real space. In Figure 9a, Kramers-Weyl points with positive and negative chirality are indicated with red and blue points, respectively. Interestingly, among the Kramers-Weyl points near the Fermi level, the one at A-point right above the Fermi level (Figure 9b) is notable because its chiral charge is +3 (another Weyl point with a chiral charge of +1 is located directly above it within a small energy window). Figure 9c shows that the flow of WCC has winding number 3 with positive slops, demonstrating the positive charge +3 Weyl fermion. A Weyl point with a chiral charge of +3 typically gives rise to multiple Fermi arcs, whereas a chiral charge of +1 only gives one Fermi arc. However, the Weyl point with a chiral charge of +3 is buried inside the projected bands of the bulk, making it challenging to detect the multiple Fermi arcs.

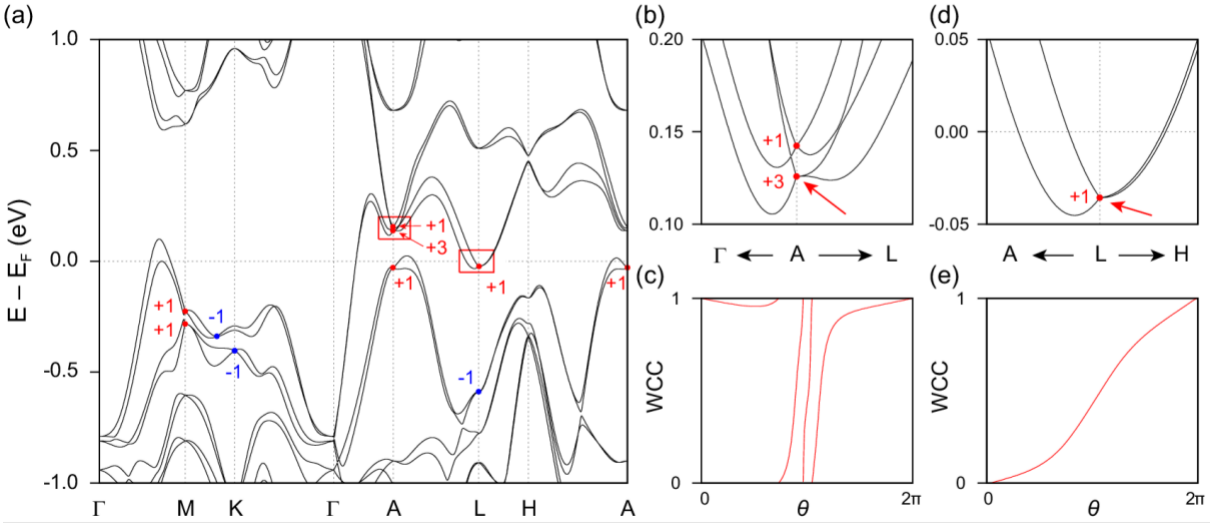

Figure 9. (a) DFT band structure of $IrGe_4$ with the space group of $P3_121$ (No. 152). The Fermi level E_F is set to zero. Kramers-Weyl points with positive and negative chirality and are indicated by red and blue points, respectively. Here, Kramers-Weyl points are presented only within an energy window of [– 0.6 eV, 0.5 eV] with respect to the Fermi level E_F. Note that there are additional non-Kramers Weyl points at K and along M-K, exhibiting negative chirality as shown in (a). (b) Enlarged band structure of the red square in (a), near A-point. Positive charge-3 Weyl point is indicated by the red arrow. (c) The flow of the Wannier charge center for the Weyl point is indicated by the red arrow in (b), demonstrating that its charge is +3. (d) Enlarged band structure of the red square in (a), near L-point. The positive charge-1 Weyl point is indicated by the red arrow. Note that the Kramers-Weyl point is slightly below the Fermi level. (e) The flow of the Wannier charge center for the Weyl point is indicated by the red arrow in (d), demonstrating that its charge is +1.

Another important aspect of the band structure shown in Figure 9a is that it possesses Kramers-Weyl points at A and L very close to the Fermi level. They have a positive charge of +1, and their energy positions are -0.03 and -0.025 eV for A and L points, respectively. Figures 9d and e show characteristics of the Kramers-Weyl point at L, where the enlarged band dispersion near the L-point and the flow of WCC for the corresponding Kramers-Weyl point are demonstrated. Figure 9e shows winding number 1 with a positive slope, thereby presenting that the Kramers-Weyl point at the L-

point has a positive charge of +1. Furthermore, in order to show features of the Kramers-Weyl points at A and L points (Figures 9b and d) more apparently, we present their band dispersions with a different color for a different band index along Γ – A – Γ and A – L – A directions, respectively (Figure S4). It is worth noting that the band structures obtained from both DFT and Wannierization methods are essentially the same (Figure S5). This enables the adoption of the symmetrized Wannier method for computing chiral charges for the Kramers-Weyl points.[47] A comparison between the band structures of space groups $P3_1$ (No. 144) and $P3_121$ (No. 152) is presented in Figure S6. In contrast to the $P3_1$ band structure (Figure S6a), the $P3_121$ band structure (Figure S6b) exhibits the presence of an additional twofold rotation symmetry along the [110] axis, resulting in multiple irreducible representations for generic k-points along the *M-K* path. This leads to accidental band crossings. The red arrow in Figure S6b highlights a new band crossing protected by this additional crystal symmetry. Aside from this distinction, both band structures exhibit nearly identical band structures, particularly with respect to the presence of Weyl points at TRIMs.

CONCLUSION

Phase-pure polycrystalline $IrGe_4$ sample has been successfully prepared with the solid-state method. Even though it is not possible to distinguish the NCS space groups $P3_1$ and $P3_121$ based on PXRD patterns, SAED, or even HAADF-STEM, we found that CBED is a powerful method to confirm the chiral crystal structure, particularly when the polar and chiral crystal structure is very close to related chiral crystal structure. $IrGe_4$ is a Weyl metal according to the DFT calculations, and additional experiments, such as an angle-resolved photoemission spectroscopy experiment on a single crystal, would be needed to verify the Weyl behavior in this compound. $IrGe_4$ is the first example of NCS chiral Weyl metal in the Ir-Ge system and another example of NCS Ir-containing topological semimetal in addition to the previous report of $MIrTe_4$ (M = Nb, Ta). Therefore, $IrGe_4$ enriches the library of limited Ir-containing topological Weyl or Dirac metals/semimetals. The study of $IrGe_4$ can be useful for investigating other Ir-containing topological materials.

ASSOCIATED CONTENT

Supporting Information. Crystal structure of $IrGe_4$ (space group $P3_1$); DFT band structure of $IrGe_4$ (space group $P3_121$) with (a) and without (b) SOC; Weyl Fermions in the Brillouin zone; Weyl Fermions in the Brillouin zone; Band structure comparison between DFT and Wannierization; DFT band structures of $IrGe_4$ with the space groups (a) $P3_1$ (No. 144) and (b) $P3_121$ (No. 152) including SOC.

AUTHOR INFORMATION

Corresponding Authors* E-mail: xtan6@gmu.edu; cjkang87@cnu.ac.kr.

ACKNOWLEDGMENTS

C. M. S. and X. T. were supported by start-up funding from George Mason University. H. B. and N. J. G acknowledge the support from the National Science Foundation (NSF.) CAREER award DMR-2143903. D. -C. R. and C. -J. K. were supported by the National Research Foundation of Korea (NRF) grant (NRF-2022R1C1C1008200). C.-J. K. was also supported by the Korea Institute of Science and Technology Information (KISTI) Supercomputing Center (Project No. KSC-2022-CRE-0438). TEM

work was performed at the National High Magnetic Field Laboratory, which is supported by National Science Foundation Cooperative Agreement No. DMR-1644779 and the State of Florida. Use of the Advanced Photon Source at Argonne National Laboratory was supported by the U. S. Department of Energy, Office of Science, Office of Basic Energy Sciences, under Contract No. DE-AC02-06CH11357. We thank Dr. David Walker (Columbia University) for pressing the dense pellet under high pressure.

REFERENCES

(1) Kumar, N.; Guin, S. N.; Manna, K.; Shekhar, C.; Felser, C. Topological Quantum Materials from the Viewpoint of Chemistry. *Chem. Rev.* **2021**, *121*, 2780–2815.

(2) Burkov, A. A. Weyl Metals. *Annu. Rev. Condens. Matter Phys.* **2018**, *9*, 359–378.

(3) Son, D. T.; Spivak, B. Z. Chiral Anomaly and Classical Negative Magnetoresistance of Weyl Metals. *Phys. Rev. B* **2013**, *88*, 104412.

(4) Arnold, F.; Shekhar, C.; Wu, S. C.; Sun, Y.; Dos Reis, R. D.; Kumar, N.; Naumann, M.; Ajeesh, M. O.; Schmidt, M.; Grushin, A. G.; Bardarson, J. H.; Baenitz, M.; Sokolov, D.; Borrmann, H.; Nicklas, M.; Felser, C.; Hassinger, E.; Yan, B. Negative Magnetoresistance without Well-Defined Chirality in the Weyl Semimetal TaP. *Nat. Commun.* **2016**, *7*, 11615.

(5) Nielsen, H. B.; Ninomiya, M. The Adler-Bell-Jackiw Anomaly and Weyl Fermions in a Crystal. *Phys. Lett. B* **1983**, *130*, 389–396.

(6) Xu, Gang; Weng, Hongming; Wang, Zhijun; Dai, Xi; Fang, Z. Chern Semimetal and the Quantized Anomalous Hall Effect in $HgCr_2Se_4$. *Phys. Rev. Lett.* **2011**, *107*, 186806.

(7) Shekhar, C.; Nayak, A. K.; Sun, Y.; Schmidt, M.; Nicklas, M.; Leermakers, I.; Zeitler, U.; Skourski, Y.; Wosnitza, J.; Liu, Z.; Chen, Y.; Schnelle, W.; Borrmann, H.; Grin, Y.; Felser, C.; Yan, B. Extremely Large Magnetoresistance and Ultrahigh Mobility in the Topological Weyl Semimetal Candidate NbP. *Nat. Phys.* **2015**, *11*, 645–649.

(8) Ghimire, N. J.; Luo, Y.; Neupane, M.; Williams, D. J.; Bauer, E. D.; Ronning, F. Magnetotransport of Single Crystalline NbAs. *J. Phys. Condens. Matter* **2015**, *27*, 152201.

(9) Xu, S. Y.; Belopolski, I.; Alidoust, N.; Neupane, M.; Bian, G.; Zhang, C.; Sankar, R.; Chang, G.; Yuan, Z.; Lee, C. C.; Huang, S. M.; Zheng, H.; Ma, J.; Sanchez, D. S.; Wang, B.; Bansil, A.; Chou, F.; Shibayev, P. P.; Lin, H.; Jia, S.; Hasan, M. Z. Discovery of a Weyl Fermion Semimetal and Topological Fermi Arcs. *Science* **2015**, *349*, 613–617.

(10) Jiang, J.; Liu, Z. K.; Sun, Y.; Yang, H. F.; Rajamathi, C. R.; Qi, Y. P.; Yang, L. X.; Chen, C.; Peng, H.; Hwang, C. C.; Sun, S. Z.; Mo, S. K.; Vobornik, I.; Fujii, J; Parkin, S. S. P.; Felser, C.; Yan, B. H.; Chen, Y. L. Signature of Type-II Weyl Semimetal Phase in $MoTe_2$. *Nat. Commun.* **2017**, *8*, 13973.

(11) Pan, Y.; He, B.; Helm, T.; Chen, D.; Schnelle, W.; Felser, C. Ultrahigh Transverse Thermoelectric Power Factor in Flexible Weyl Semimetal WTe_2. *Nat. Commun.* **2022**, *13*, 3909.

(12) Li, P.; Koo, J.; Ning, W.; Li, J.; Miao, L.; Min, L.; Zhu, Y.; Wang, Y.; Alem, N.; Liu, C. X.; Mao, Z.; Yan, B. Giant Room Temperature Anomalous Hall Effect and Tunable Topology in a Ferromagnetic Topological Semimetal Co_2MnAl. *Nat. Commun.* **2020**, *11*, 3476.

(13) Safi, T. S.; Chou, C. T.; Hou, J. T.; Han, J.; Liu, L. Spin-Generation in Magnetic Weyl Semimetal Co_2MnGa across Varying Degree of Chemical Order. *Appl. Phys. Lett.* **2022**, *121*, 092404.

(14) Xu, S. Y.; Alidoust, N.; Chang, G.; Lu, H.; Singh, B.; Belopolski, I.; Sanchez, D. S.; Zhang, X.; Bian, G.; Zheng, H.; Husanu, M. A.; Bian, Y.; Huang, S. M.; Hsu, C. H.; Chang, T, R.; Jeng, H. T.; Bansil, A.; Neupert, T.; Strocov, V. N.; Lin, H.; Jia, S. Hasan, M. Z. Discovery of Lorentz-

Violating Type II Weyl Fermions in LaAlGe. *Sci. Adv.* **2017**, *3*, e1603266.
(15) Wang, J. F.; Dong, Q. X.; Guo, Z. P.; Lv, M.; Huang, Y. F.; Xiang, J. Sen; Ren, Z. A.; Wang, Z. J.; Sun, P. J.; Li, G.; Chen, G. F. NdAlSi: A Magnetic Weyl Semimetal Candidate with Rich Magnetic Phases and Atypical Transport Properties. *Phys. Rev. B* **2022**, *105*, 144435.
(16) Huber, N.; Alpin, K.; Causer, G. L.; Worch, L.; Bauer, A.; Benka, G.; Hirschmann, M. M.; Schnyder, A. P.; Pfleiderer, C.; Wilde, M. A. Network of Topological Nodal Planes, Multifold Degeneracies, and Weyl Points in CoSi. *Phys. Rev. Lett.* **2022**, *129*, 026401.
(17) Meng, W.; Zhang, X.; He, T.; Jin, L.; Dai, X.; Liu, Y.; Liu, G. Ternary Compound HfCuP: An Excellent Weyl Semimetal with the Coexistence of Type-I and Type-II Weyl Nodes. *J. Adv. Res.* **2020**, *24*, 523–528.
(18) Ge, Y.; Jin, Y.; Zhu, Z. Ferromagnetic Weyl Metal in EuAgP. *Mater. Today Phys.* **2022**, *22*, 100570.
(19) Zeng, Q.; Yi, C.; Shen, J.; Wang, B.; Wei, H.; Shi, Y.; Liu, E. Berry Curvature Induced Antisymmetric In-Plane Magneto-Transport in Magnetic Weyl EuB_6. *Appl. Phys. Lett.* **2022**, *121*, 162405.
(20) Wilde, J. M.; Riberolles, S. X. M.; Das, A.; Liu, Y.; Heitmann, T. W.; Wang, X.; Straszheim, W. E.; Bud'ko, S. L.; Canfield, P. C.; Kreyssig, A.; McQueeney, R. J.; Ryan, D. H., Ueland, B. G. Canted Antiferromagnetic Phases in the Candidate Layered Weyl Material $EuMnSb_2$. *Phys. Rev. B* **2022**, *106*, 024420.
(21) Ni, X. S.; Chen, C. Q.; Yao, D. X.; Hou, Y. Origin of the Type-II Weyl State in Topological Antiferromagnetic $YbMnBi_2$. *Phys. Rev. B* **2022**, *105*, 134406.
(22) Kuroda, K.; Tomita, T.; Suzuki, M. T.; Bareille, C.; Nugroho, A. A.; Goswami, P.; Ochi, M.; Ikhlas, M.; Nakayama, M.; Akebi, S.; Noguchi, R.; Ishii, R.; Inami, N.; Ono, K.; Kumigashira, H.; Varykhalov, A.; Muro, T.; Koretsune, T.; Arita, R.; Shin, S.; Kondo, T.; Nakatsuji, S. Evidence for Magnetic Weyl Fermions in a Correlated Metal. *Nat. Mater.* **2017**, *16*, 1090–1095.
(23) Chen, T.; Tomita, T.; Minami, S.; Fu, M.; Koretsune, T.; Kitatani, M.; Muhammad, I.; Nishio-Hamane, D.; Ishii, R.; Ishii, F.; Arita, R.; Nakatsuji, S. Anomalous Transport Due to Weyl Fermions in the Chiral Antiferromagnets Mn_3X, X = Sn, Ge. *Nat. Commun.* **2021**, *12*, 572.
(24) Rossi, A.; Ivanov, V.; Sreedhar, S.; Gross, A. L.; Shen, Z.; Rotenberg, E.; Bostwick, A.; Jozwiak, C.; Taufour, V.; Savrasov, S. Y.; Vishik, I. M. Electronic Structure and Topology across T_c in the Magnetic Weyl Semimetal $Co_3Sn_2S_2$. *Phys. Rev. B* **2021**, *104*, 155115.
(25) Kumar, D.; Hsu, C. H.; Sharma, R.; Chang, T. R.; Yu, P.; Wang, J.; Eda, G.; Liang, G.; Yang, H. Room-Temperature Nonlinear Hall Effect and Wireless Radiofrequency Rectification in Weyl Semimetal $TaIrTe_4$. *Nat. Nanotechnol.* **2021**, *16*, 421–425.
(26) Zhang, J.; Zhang, T.; Yan, L.; Zhu, C.; Shen, W.; Hu, C.; Lei, H.; Luo, H.; Zhang, D.; Liu, F.; Liu, Z.; Tong, J.; Zhou, L.; Yu, P.; Yang, G. Colossal Room-Temperature Terahertz Topological Response in Type-II Weyl Semimetal $NbIrTe_4$. *Adv. Mater.* **2022**, *34*, 2204621.
(27) Khoury, J. F.; Rettie, A. J. E.; Khan, M. A.; Ghimire, N. J.; Robredo, I.; Pfluger, J. E.; Pal, K.; Wolverton, C.; Bergara, A.; Jiang, J. S.; Schoop, L. M.; Vergniory, M. G.; Mitchell, J. F.; Chung, D. Y.; Kanatzidis, M. G. A New Three-Dimensional Subsulfide Ir_2In_8S with Dirac Semimetal Behavior. *J. Am. Chem. Soc.* **2019**, *141*, 19130–19137.
(28) Khoury, J. F.; Rettie, A. J. E.; Robredo, I.; Krogstad, M. J.; Malliakas, C. D.; Bergara, A.; Vergniory, M. G.; Osborn, R.; Rosenkranz, S.; Chung, D. Y.; Kanatzidis, M. G. The Subchalcogenides Ir_2In_8Q (Q = S, Se, Te): Dirac Semimetal Candidates with Re-Entrant Structural Modulation. *J. Am. Chem. Soc.* **2020**, *142*, 6312–6323.
(29) Fei, F.; Bo, X.; Wang, P.; Ying, J.; Li, J.; Chen, K.; Dai, Q.; Chen, B.; Sun, Z.; Zhang, M.; Qu, F.;

Zhang, Y.; Wang, Q.; Wang, X.; Cao, L.; Bu, H.; Song, F.; Wan, X.; Wang, B. Band Structure Perfection and Superconductivity in Type-II Dirac Semimetal $Ir_{1-x}Pt_xTe_2$. *Adv. Mater.* **2018**, *30*, 1801556.

(30) Jiang, J.; Lee, S.; Fei, F.; Song, F.; Vescovo, E.; Kaznatcheev, K.; Walker, F. J.; Ahn, C. H. A Comprehensive ARPES Study on the Type-II Dirac Semimetal Candidate $Ir_{1-x}Pt_xTe_2$. *APL Mater.* **2020**, *8*, 061106.

(31) Pfisterer, Hermann; Schubert, K. New Phases of MnP (B31) Type. *Naturwissenschaften* **1950**, *37*, 112–113.

(32) Panday, Prabhat K.; Singh, Gouri S. P.; Schubert, K. Kristallstruktur von Ir_4Ge_5. *Zeitschrift fuer Krist.* **1967**, *125*, 274–285.

(33) Flieher, G.; Voellenkle, H.; Nowotny, H. Die Kristallstruktur von Ir_4Ge_5. *Monatshefte fuer Chemie* **1968**, *99*, 877–883.

(34) Schubert, Konrad; Pfisterer, H. Crystal Chemistry of Alloys of Elements of the Iron and Platinum Triads with Elements of the IV B Group. *Zeitschrift fuer Met.* **1950**, *41*, 433–441.

(35) Panday, Prabhat K.; Schubert, K. Structure Studies in Some T-B^3-B^4 Mixtures (T = Mn, Fe, Co, Ir, Ni, Pd; B^3 = Al, Ga, Tl; B^4 = Si, Ge). *J. Less-Common Met.* **1969**, *18*, 175–202.

(36) Schubert, Konrad; Bhan, Suraj; Biswas, Tapash K.; Frank, Konrad; Panday, P. K. Structural Data of Metallic Phases. XIII. *Naturwissenschaften* **1968**, *55*, 542–543.

(37) Chang, G.; Wieder, B. J.; Schindler, F.; Sanchez, D. S.; Belopolski, I.; Huang, S. M.; Singh, B.; Wu, D.; Chang, T. R.; Neupert, T.; Xu, S. Y.; Lin, H.; Hasan, M. Z. Topological Quantum Properties of Chiral Crystals. *Nat. Mater.* **2018**, *17*, 978–985.

(38) Matthias, B. T. Superconducting Compounds of Nonsuperconducting Elements. *Phys. Rev.* **1950**, *90*, 487.

(39) Hirai, D.; Ali, M. N.; Cava, R. J. Strong Electron-Phonon Coupling Superconductivity Induced by a Low-Lying Phonon in IrGe. *Jounral Phys. Soc. Japan* **2013**, *82*, 124701.

(40) Rodríguez-Carvajal, Juan. Recent Advances in Magnetic Structure Determination by Neutron Powder Diffraction. *Phys. B Condens. Matter* **1993**, *192*, 55–69.

(41) Kresse, Georg; Joubert, D. From Ultrasoft Pseudopotentials to the Projector Augmented-Wave Method. *Phys. Rev. B* **1999**, *59*, 1758.

(42) Kresse, G.; Furthmüller, J. Efficiency of Ab-Initio Total Energy Calculations for Metals and Semiconductors Using a Plane-Wave Basis Set. *Comput. Mater. Sci.* **1996**, *6*, 15–50.

(43) Kresse, G.; Furthmüller, J. Efficient Iterative Schemes for Ab Initio Total-Energy Calculations Using a Plane-Wave Basis Set. *Phys. Rev. B - Condens. Matter Mater. Phys.* **1996**, *54*, 11169–11186.

(44) Perdew, J. P.; Burke, K.; Ernzerhof, M. Generalized Gradient Approximation Made Simple. *Phys. Rev. Lett.* **1996**, *77*, 3865–3868.

(45) Mostofi, A. A.; Yates, J. R.; Pizzi, G.; Lee, Y. S.; Souza, I.; Vanderbilt, D.; Marzari, N. An Updated Version of Wannier90: A Tool for Obtaining Maximally-Localised Wannier Functions. *Comput. Phys. Commun.* **2014**, *185*, 2309–2310.

(46) Wu, Q. S.; Zhang, S. N.; Song, H. F.; Troyer, M.; Soluyanov, A. A. WannierTools: An Open-Source Software Package for Novel Topological Materials. *Comput. Phys. Commun.* **2018**, *224*, 405–416.

(47) Gresch, D.; Wu, Q.; Winkler, G. W.; Häuselmann, R.; Troyer, M.; Soluyanov, A. A. Automated Construction of Symmetrized Wannier-like Tight-Binding Models from Ab Initio Calculations. *Phys. Rev. Mater.* **2018**, *2*, 103805.

(48) Hellner, E.; Koch, E. A Comparison of the Crystal Structures of antimony-thallium (Sb_2Tl_7),

copper-zinc (Cu_5Zn_8) (γ-Brass), and Ir_3Ge_7. *Can. J. Chem* **1985**, *58*, 708–713.
(49) Christensen, M.; Johnsen, S.; Iversen, B. B. Thermoelectric Clathrates of Type I. *Dalt. Trans.* **2010**, *39*, 978–992.
(50) Rodewald, Ute Ch.; Pottgen, R. Three-Dimensional Iridium-Germanium Polyanions in the Structures of Yb_2IrGe_2, LuIrGe, and $Lu_3Ir_2Ge_3$. *Solid State Sci.* **2003**, *5*, 487–493.
(51) Goodman, P. A Practical Method of Three-Dimensional Space-Group Analysis Using Convergent-Beam Electron Diffraction. *Acta Crystallogr. Sect. A Found. Adv.* **1975**, *A31*, 804–810.
(52) Tanaka, M.; Saito, R.; Sekii, H. Point-Group Determination by Convergent-Beam Electron Diffraction. *Acta Crystallogr. Sect. A Found. Adv.* **1983**, *A39*, 357–368.
(53) Steeds, J. W.; Vincent, R. Use of High-Symmetry Zone Axes in Electron Diffraction in Determining Crystal Point and Space Groups. *J. Appl. Cryst.* **1983**, *16*, 317–324.
(54) Williams, D. B.; Carter, C. B. *Transmission Electron Microscopy: A Textbook for Materials Science*; Plenum Press, New York and London, P332, 1996.
(55) Nakamura, Naoki; Yanuma, Ayano; Chiba, Yuma; Omura, Rumi; Higashinaka, Ryuji; Harima, Hisatomo; Aoki, Yuji; Matsuda, Tatsuma, D. Fermi Surface and Superconducting Properties of α-$IrSn_4$, α-$RhSn_4$, $IrGe_4$, and $RhGe_4$ with Trigonal Chiral Structure. *J. Phys. Soc. Jpn.* **2023**, *92*, 034701.
(56) Ghimire, N. J.; Botana, A. S.; Jiang, J. S.; Zhang, J.; Chen, Y. S.; Mitchell, J. F. Large Anomalous Hall Effect in the Chiral-Lattice Antiferromagnet $CoNb_3S_6$. *Nat. Commun.* **2018**, *9*, 3280.
(57) Fecher, G. H.; Kübler, J.; Felser, C. Chirality in the Solid State: Chiral Crystal Structures in Chiral and Achiral Space Groups. *Materials.* **2022**, *15*, 5812.
(58) Hautier, G.; Ong, S. P.; Jain, A.; Moore, C. J.; Ceder, G. Accuracy of Density Functional Theory in Predicting Formation Energies of Ternary Oxides from Binary Oxides and Its Implication on Phase Stability. *Phys. Rev. B - Condens. Matter Mater. Phys.* **2012**, *85*, 155208.
(59) Soluyanov, A. A.; Gresch, D.; Wang, Z.; Wu, Q.; Troyer, M.; Dai, X.; Bernevig, B. A. Type-II Weyl Semimetals. *Nature* **2015**, *527*, 495–498.

For Table of Contents Only

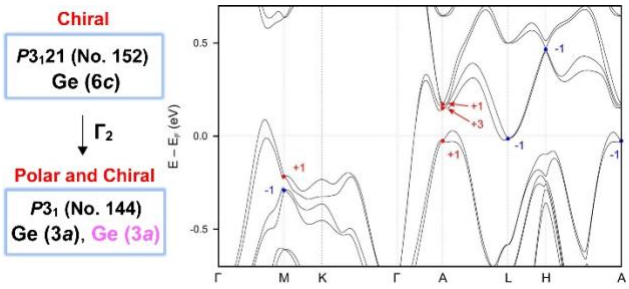

$IrGe_4$ adopts a chiral crystal structure and is predicted to be a Weyl metal with a chiral charge of +3 Weyl point above the Fermi level.